Acta Materialia 303 (2026) 121683

Contents lists available at ScienceDirect

Acta Materialia

journal homepage: www.elsevier.com/locate/actamat

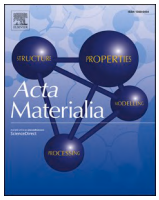

Origin of the trade-off relationship between tensile strength and hydrogen embrittlement resistance

Kazuho Okada [a,b,*], Yukihisa Watase [c], Myeong-heom Park [b], Kaneaki Tsuzaki [a], Akinobu Shibata [a]

[a] Research Center for Structural Materials, National Institute for Materials Science (NIMS), 1-2-1 Sengen, Tsukuba, Ibaraki 305-0047, Japan
[b] Department of Materials Science and Engineering, Kyoto University, Yoshida- honmachi, Sakyo-ku, Kyoto 606-8501, Japan
[c] Solution Development Center, Solution Promotion Department, JEOL Ltd, 3-1-2 Musashino, Akishima, Tokyo 196-8558, Japan

ARTICLE INFO

Keywords:
Hydrogen embrittlement
Martensitic steel
Intergranular failure
Stress localization
Digital image correlation (DIC)

ABSTRACT

To achieve widespread application of high-strength steels, such as martensitic steels, understanding the origin of the trade-off relationship between tensile strength and hydrogen embrittlement resistance is crucial. This study aimed to clarify the origin of the trade-off from a perspective of sensitivity to the hydrogen-induced intergranular fracture, which mainly occurs along prior austenite grain boundaries (PAGBs) among several types of high-angle boundaries in martensitic structures. Applying a digital image correlation (DIC)-based stress mapping technique, the distribution of the local stress during tensile loading was correlated with the martensitic structures; the stress concentration behaviors at PAGBs were compared among three as-quenched martensitic steels with different tensile strengths. The tensile strength, ranging from 1.25 to 1.65 GPa, was controlled by changing carbon composition and austenitization temperature (and resultant PAG size) in Fe-3Mn-C (wt.%) alloys. The intergranular fracture preferentially occurring at PAGBs is due to the low plastic relaxation ability of PAGBs relative to other substructure boundaries (within PAGs) and the resultant stress concentration at PAGBs. Additionally, it was demonstrated that as plastic relaxation at PAGBs crystallographically becomes more difficult relative to within PAGs, the consequent stress concentration at PAGBs increases, leading to more severe hydrogen embrittlement. The results demonstrated both the origin of the trade-off (i.e., carbon composition) and a strategy for breaking the trade-off (i.e., PAG refinement), and both can be understood in terms of the shared factors: sensitivity to the intergranular fracture, strongly depending on the local stress concentration at PAGBs related to variant selection behavior in the martensitic transformation.

1. Introduction

Commercializing structural materials with as high strength as possible is crucial to enlarging architectural structures and improving fuel efficiency by reducing the weight of transportation equipment such as automobiles. However, steel, the most widely used metallic material, becomes increasingly susceptible to hydrogen embrittlement as its strength level increases. The trade-off relationship between strength level and hydrogen embrittlement resistance is evident when the tensile strength (*TS*) exceeds ~1.2 GPa [1]. Hydrogen embrittlement is the phenomenon by which hydrogen deteriorates the mechanical properties of a material [2–8]. Since absorbing a certain amount of hydrogen into steels during fabrication and application is unavoidable, there has been a strong and persistent demand to establish materials design guidelines for overcoming the trade-off relationship.

Martensitic steels, representative low/medium-carbon high-strength steels, show high susceptibility to hydrogen embrittlement. Quasi-cleavage (transgranular) and intergranular fractures are the typical hydrogen-induced fracture modes in martensitic steels. Generally, intergranular fracture becomes dominant as the hydrogen content increases, leading to more severe embrittlement [9]. Therefore, the primary focus in overcoming hydrogen embrittlement is to suppress intergranular fracture. This study aimed to clarify the origin of the trade-off from a perspective of sensitivity to the hydrogen-induced intergranular fracture. In the martensitic transformation, twenty-four equivalent crystallographic variants (V) can be transformed from a

* Corresponding author.
E-mail addresses: okada.kazuho@nims.go.jp (K. Okada), ywatase@jeol.co.jp (Y. Watase), park.myeongheom.8r@kyoto-u.ac.jp (M.-h. Park), tsuzaki.kaneaki@emeritus.nims.go.jp (K. Tsuzaki), shibata.akinobu@nims.go.jp (A. Shibata).

https://doi.org/10.1016/j.actamat.2025.121683
Received 1 April 2025; Received in revised form 22 October 2025; Accepted 27 October 2025
Available online 30 October 2025

single parent austenite grain, satisfying the Kurdjumov-Sachs (K-S) orientation relationship. Consequently, a prior austenite grain is subdivided into several structural units with different size scales, namely lath, block, and packet. Lath boundaries are low-angle boundaries, while block boundaries, packet boundaries, and prior austenite grain boundaries (PAGBs) are basically high-angle boundaries [10–14]. A PAGB is an austenite grain boundary at high temperatures that has been subdivided by the martensitic transformation into numerous segmented boundaries of adjoining martensite variants with varying misorientations. Despite the existence of these several types of high-angle boundaries, hydrogen preferentially accumulates to PAGBs during deformation, thereby the hydrogen-induced intergranular fracture mainly occurs along PAGBs [15–22]. Hydrogen-induced reduction of the PAGB cohesive energy leads to intergranular decohesion [23–25]. However, the reason why hydrogen preferentially accumulates to PAGB is not understood.

To date, microstructural control strategies to suppress hydrogen-induced intergranular fracture have been proposed extensively in martensitic steels, such as increasing carbon segregation at PAGB [26–28], precipitating nano-carbides [29–35], and chemical heterogeneity [36], etc. However, these previous studies have not fundamentally resolved the underlying origin of the trade-off relationship between the *TS* and hydrogen resistance. For example, Okada et al. [26] produced two martensitic steels from a single ingot, with only the segregated carbon concentration at the PAGB differing between them. They demonstrated that carbon segregation at PAGB increased the PAGB cohesive energy and suppressed the hydrogen-induced intergranular fracture. However, when martensitic steels are produced from ingots with different chemical compositions, steels with higher *TS* basically have greater carbon compositions, resulting in a higher equilibrium carbon concentration at PAGB and thus a higher PAGB cohesive energy. Consequently, if carbon segregation at PAGB is the underlying origin of the trade-off relationship, it would suggest that steels with higher *TS* have greater resistance to the hydrogen-induced intergranular fracture. Conflictingly, this is exactly the opposite of the real trade-off relationship. Therefore, solute segregation at PAGB, i.e., PAGB cohesive energy, is not the origin of the trade-off relationship.

The intergranular fracture occurs when local stress imposed on PAGB exceeds the threshold required for PAGB decohesion. Namely, a balance between the local stress imposed on PAGB and PAGB cohesive energy determines the local fracture criteria. As explained above, PAGB cohesive energy is not the origin of the trade-off relationship. Thus, the local stress imposed on PAGB is key to revealing the origin of the trade-off relationship. Wang et al. [37,38] performed uniaxial tensile tests using notched-bar specimens with different stress concentration factors and different bulk average diffusible hydrogen contents (H_D). They demonstrated that the relationship between the local fracture stress (maximum principal stress) and the local hydrogen concentration at the crack initiation site (notch root area) was independent of the stress concentration factor and H_D, supporting the importance of local stress value. However, they also reported that the relationships between the local fracture stress and the local hydrogen concentration changed depending on the *TS*; thus, it was still not able to explain the trade-off relationship. Their finite element simulations only evaluated the local stress based on macroscopic stress concentrations caused by the specimen geometry, without considering the stress concentrations originating from the microstructure, specifically the local stress concentration at PAGBs.

In the present study, we performed uniaxial tensile tests using smooth specimens without notches and evaluated the local stress/strain concentration at PAGBs using the digital image correlation (DIC) method. Comparing three as-quenched martensitic steels with different *TS* and different resistance against hydrogen-induced intergranular fracture, the origin of the trade-off relationship between the *TS* and hydrogen embrittlement resistance was revealed from the perspective of local stress/strain concentration, and further the variant selection of martensitic transformation, at PAGBs. The *TS*, ranging from 1.25 to 1.65 GPa, was controlled by changing carbon composition and austenitization temperature (and resultant PAG size) in Fe-3Mn-C (wt. %) alloys. These factors are the most common dominant factors governing the *TS* of martensitic steels. It should be noted that the PAGB segregation of alloying elements other than carbon, such as manganese, was not observed in this alloy [26]; therefore, we simply focused on the stress/strain concentration at PAGBs in this study.

2. Experimental

2.1. Materials

Fe-3Mn-0.1C/0.2C alloys were used in the present study. The detailed chemical compositions (wt. %) are Mn: 2.99, C: 0.103, Si: 0.01, P: <0.002, S: 0.0012, Al: 0.0012, N: 0.0028, O: 0.0024, and Fe: balance for the Fe-3Mn-0.1C alloy, and Mn: 3.02, C: 0.18, Si: 0.01, P: <0.002, S: 0.001, Al: 0.002, N: 0.002, O: 0.001, and Fe: balance for the Fe-3Mn-0.2C alloy. The hot-rolled plates were austenitized, ice brine quenched, and sub-zero cooled in liquid nitrogen for 10 min. The austenitizations were conducted at 900 °C for 30 min for the Fe-3Mn-0.1C alloy, and at 900 or 1100 °C for 30 min for the Fe-3Mn-0.2C alloy. For optical microscopy observation, the specimens were mechanically wet-polished using emery paper up to #4000, electrochemically polished in an aqueous solution of 50 ml $HCLO_4$ + 450 ml CH_3COOH at 22 V for 90 s at ambient temperature, and then etched in a 3 % nital solution. The PAG sizes, measured by the line-interception method, were 65, 62, and 183 μm in the 3Mn-0.1C alloy austenitized at 900 °C, 3Mn-0.2C alloy austenitized at 900 °C, and 3Mn-0.2C alloy austenitized at 1100 °C, respectively. We refer to the three types of specimens mentioned above in the same order as 0.1C_65μm, 0.2C_62μm, and 0.2C_183μm specimens, respectively.

2.2. Hydrogen embrittlement behaviors

Sheet-type smooth specimens (gauge width: 2 mm, gauge length: 10 mm, and gauge thickness: 0.25 ~ 2.0 mm) and pre-cracked compact tension (CT) specimens (thickness: 12.5 mm, width: 25 mm, and net thickness at the side grooves' root: 10 mm) were prepared from the heat-treated specimens. Sheet-type smooth specimens with 1.0 mm thickness and pre-cracked CT specimens were cathodically pre-charged with hydrogen in an aqueous solution containing 3 % NaCl + 3 g L^{-1} NH_4SCN for 24 h or 72 h, respectively, at room temperature. We have confirmed that 24 or 72 h of charging was sufficient to achieve a uniform hydrogen distribution within the present specimen geometries, as the H_D reached saturation before 24 or 72 h and did not increase with charging periods longer than 24 or 72 h. To obtain the specimens with different H_D, the current density of the hydrogen charging was changed from 0 to 5 A m^{-2}. The H_D was measured by thermal desorption spectroscopy (TDS) using a quadrupole mass (Q-mass) spectrometer (R-DEC: HTDS-004) at a heating rate of 100 °C h^{-1}. The content of hydrogen desorbed below 400 °C was regarded as the H_D. As shown in **Fig. S1**, the H_D increased with the current density up to 3 A m^{-2}, while it was saturated above 3 A m^{-2}. Therefore, uniaxial tensile tests were conducted on sheet-type smooth specimens pre-charged at 0 ~ 3 A m^{-2} at an initial strain rate of 8.3 × 10^{-6} s^{-1} at ambient temperature in air. Both the tensile tests and TDS measurements were started 40 min after the pre-chargings were completed. Unloading compliance tests based on the single specimen test method of ASTM E1820 were conducted on pre-cracked CT specimens (0.2C_183μm, pre-charged at 0.005 A m^{-2}) under concurrent hydrogen-charging conditions at the same current densities as the pre-charging. The crack mouth opening displacement rate and the displacement interval for unload/reload sequences were 1.0 × 10^{-4} mm s^{-1} and 0.0070 mm, respectively. The crack extension (Δa) can be obtained from the change in elastic compliance in accordance with ASTM E1820. Details of the unloading compliance tests can be found in our previous work [28].

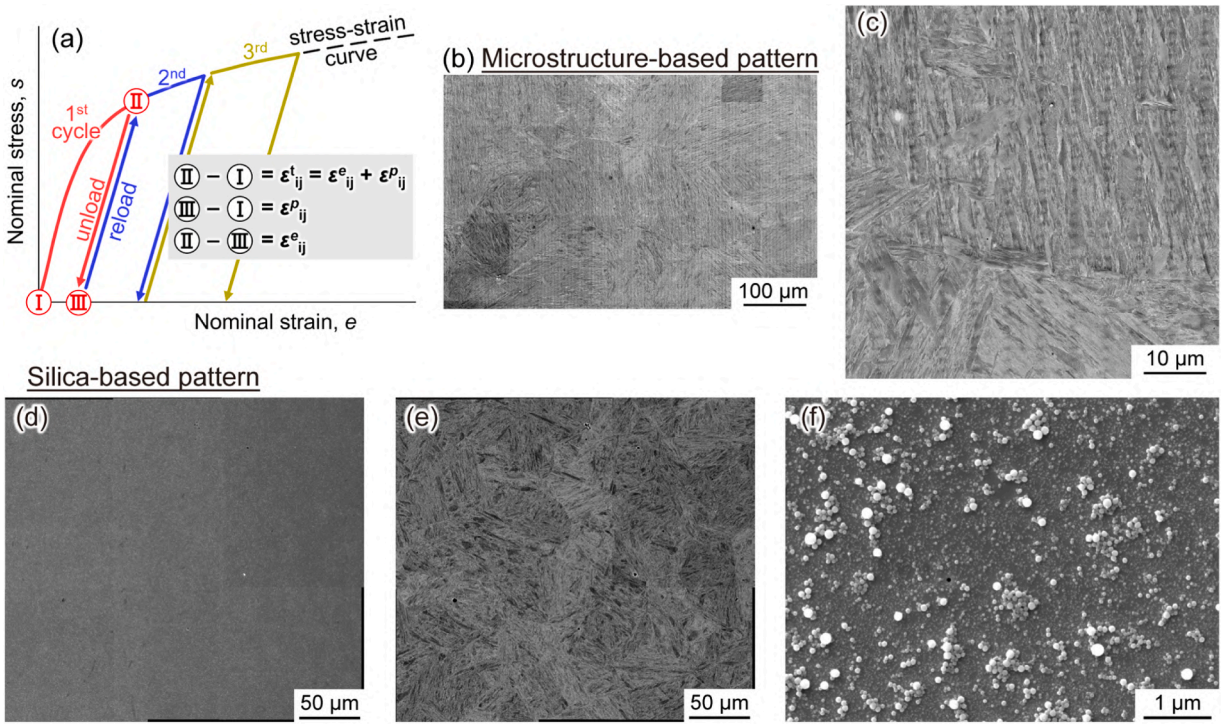

Fig. 1. Details of the present DIC analyses. (a) Schematic illustration showing the basic principle of the stress evaluation in the advanced DIC analysis. (b, c) Example of the images used for microstructure-based DIC analysis in the 0.2C_183μm specimen: (b) montage of the seventy-two SE images and (c) enlarged view of (b). (d–f) Example of the images used for silica pattern-based DIC analysis in the 0.1C_65μm specimen: (d) montage of the six SE images, (e) BSE images corresponding to (d), and (f) enlarged view of (d).

2.3. Stress distribution measurement

2.3.1. Basic principle of stress distribution measurement

The stress/strain distributions were quantitatively correlated with lath martensitic structures using the digital image correlation (DIC) method. DIC is a technique for measuring strain distribution by calculating the relative displacement vector of each reference unit, i.e., subset, within images of an object before and after deformation [39–41]. Although the EBSD-Wilkinson method [42–44] is also a candidate for local stress evaluation, it is not suitable for this study. This is because the accuracy of stress measurement heavily depends on the quality of the Kikuchi pattern, which significantly deteriorates with the strain introduced by the martensitic transformation. In addition, the evaluated stress value sensitively changes depending on the reference point, which could lead to misinterpretation when comparing different as-quenched martensitic steels. In contrast, the DIC method, which uses a random pattern on the object surface, does not have the abovementioned problems. Additionally, with the recently proposed advanced DIC method [45], it has become possible to evaluate not only strain distribution but also stress distribution.

We performed *in-situ* observation during repeated tensile loading/unloading sequences in the advanced DIC method. As shown in the schematic illustration in Fig. 1(a), the relative strain at a certain nominal stress level (stage II) against before deformation (stage I) corresponds to total strain (ε^{t}_{ij}). In the same way, the relative strain after unloading (stage III) against stage I corresponds to plastic strain (ε^{p}_{ij}). Since ε^{t}_{ij} is the sum of elastic strain (ε^{e}_{ij}) and ε^{p}_{ij}, the relative strain of stage II against stage III is ε^{e}_{ij}. Stress was calculated by the following equation, supposing plane stress condition ($\sigma_{33} = \sigma_{13} = \sigma_{23} = 0$) because the DIC analysis was limited to the specimen surface.

$$\sigma_{11} = \frac{E}{1-\nu^2}\left(\varepsilon^{e}{}_{11} + \nu\varepsilon^{e}{}_{22}\right) \quad (1)$$

where E and ν are Young's modulus and Poisson's ratio, respectively. The subscripts 1, 2, and 3 denote the axes parallel to the length (loading), width, and thickness directions of the specimen's gauge section, respectively. Strictly speaking, this method cannot consider residual elastic strain, which is included in stage III. However, we believe this stress measurement method applies to the present study, in which almost all *in-situ* observations were conducted equal to or below the 0.2 % proof stresses and the effect of residual elastic strain was considered negligible. In the previous study [45], the advanced DIC method was applied to a notched specimen tensile deformed around the 0.2 % proof stress in martensitic steel. They confirmed the overall good agreement between the stress distributions evaluated by the DIC method and finite element simulation. In the present DIC analyses, two types of random patterns were selectively used according to the purpose: lath martensitic structure (Fig. 1(b, c)) and colloidal silica particles (Fig. 1(d–f)). By directly using the lath martensitic structure as a random pattern, we made it easier to correlate the obtained stress/strain distributions with the substructure boundaries, such as block, packet, and PAG boundaries. However, microstructure-based patterns cannot exclude the undesired influence on the DIC analysis [46]. For example, spatial strain resolution changes depending on the microstructure, which is not suitable for comparing different materials. Thus, we employed colloidal silica particles as random patterns to compare the three martensitic steels. We note that the uncharged specimens were used for the DIC analysis because the hydrogen-charged specimens fractured even at a low stress level (below 500 MPa). The details of the DIC procedure for each pattern are explained in the following sections.

2.3.2. Stress/strain distribution corresponding to substructure boundaries (microstructure-based pattern)

The 0.2C_183μm specimen, having the largest PAG size, was used for the DIC analysis to correlate stress/strain distribution with substructure boundaries. The surface of the tensile specimen with a thickness of 0.4 μm was finished with electrochemical polishing under the same conditions as explained above. Using scanning electron microscopy (SEM,

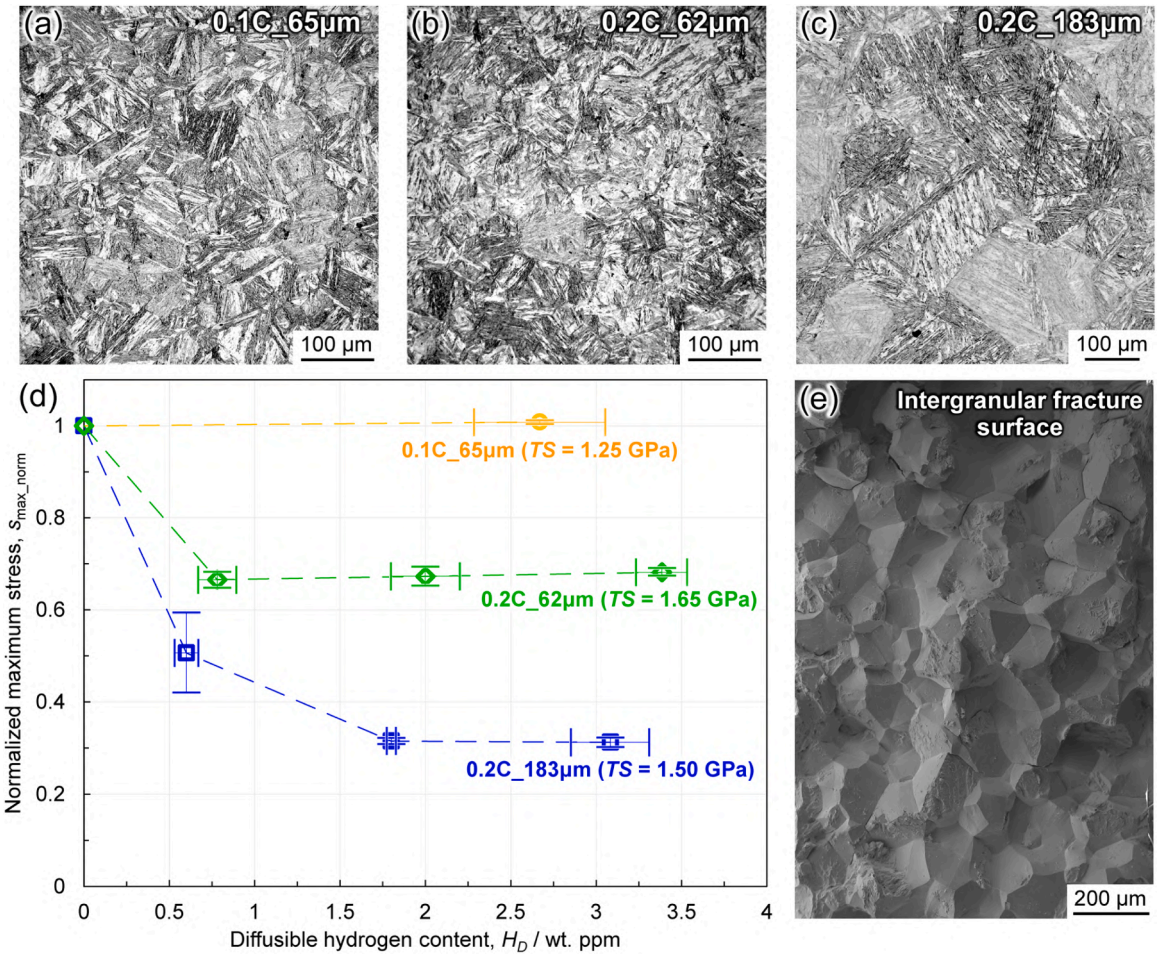

Fig. 2. Microstructures and hydrogen embrittlement behaviors of the present martensitic steels. Optical microscopy images of three as-quenched martensitic steels: (a) 3Mn-0.1C (wt. %) steel with a PAG size of 65 μm (0.1C_65μm specimen) and (b, c) 3Mn-0.2C (wt. %) steel with PAG sizes of 62 and 183 μm (0.2C_62μm and 0.2C_183μm specimens), respectively. (d) Maximum stresses normalized by the tensile strength of the uncharged specimens (s_{max_norm}) as a function of the diffusible hydrogen content (H_D). (e) SEM image of the fracture surface in the hydrogen-charged 0.2C_183μm specimen with the maximum H_D.

JEOL: JSM-IT800HL) equipped with a tensile stage (TSL Solutions), electron backscattering diffraction measurement (EBSD, step size: 0.2 μm, acceleration voltage: 15 V) was performed on a 350 × 600 μm area. The EBSD measurement and analysis were performed with the TSL OIM Data Collection program and the TSL OIM Analysis program, respectively. The PAG reconstruction was manually performed by comparing the EBSD measurement data with the ideal K–S orientation. Due to the load capacity limit of the tensile stage, the specimen thickness was set to 0.4 mm. As shown in **Fig. S2(a)**, the nominal stress–nominal strain curves before the plastic instability points did not change across a 0.25 to 2 mm thickness range. Therefore, the effect of specimen thickness on the present DIC analysis could be negligible. According to the K-S orientation relationships [9,10], the number of each martensite variant was determined. The advanced DIC analysis was performed on the area where EBSD measurements had been performed in advance, using secondary electron (SE) images observed at constant displacements corresponding to nominal stress levels of 0, 300, 600, 900, and 1200 MPa. The tensile deformation was performed at an initial strain rate of 10^{-4} s^{-1}. The displacement was held at each stress level for 60 min or more, confirming that stress relaxation was saturated (<0.5 MPa in 5 min). After that, the entire area corresponding to the EBSD orientation map was observed by capturing seventy-two SE images with 20–30 % overlap between each other, whose montage is shown in Fig. 1(b). The SEM observation was performed at an acceleration voltage of 15 kV and a current of 5 nA to obtain SE images that show the clear contrast of the lath martensitic structure, like backscattered electron (BSE) images. The contrast of the lath martensitic structure, enlarged in Fig. 1(c), was used as a random pattern for the DIC analysis. Since the signal amplification leads to increased errors in the DIC analysis, BSE images are not suitable for the present analysis where high accuracy in detecting minute strains is required. Each of the SE images has a size of 80 × 60 μm and a resolution of 1280 × 960 pixels, resulting in 1 μm corresponding to 16 pixels. Using the software VIC-2D (Correlated Solutions, Inc.), the DIC analysis was conducted at subset and step sizes of 71 and 7 pixels, respectively. In the Eq. (1), 200 GPa and 0.3 were used for E and ν, respectively. Strictly speaking, body-centered cubic (BCC) iron has large elastic anisotropy. However, since multiple variants are included within a subset (71 pixels, approximately 4.4 μm), the average elastic constants of polycrystalline BCC iron were used.

2.3.3. Quantitative comparison between three martensitic steels (silica-based pattern)

For quantitative comparison of the stress/strain concentration at PAGB between the three martensitic steels using silica-based patterns, it is necessary to minimize the contrast originating from the microstructures in SE images as much as possible. To minimize the surface roughness corresponding to the microstructure, the surface of the tensile specimen with a thickness of 0.4 μm was finished with vibration polishing with a 0.02 μm colloidal silica suspension. EBSD measurements were performed on 270 × 300 μm areas for the 0.1C_65μm and 0.2C_62μm specimens and on a 610 × 500 μm area for the 0.1C_183μm specimen. To remove contamination caused by EBSD measurements and

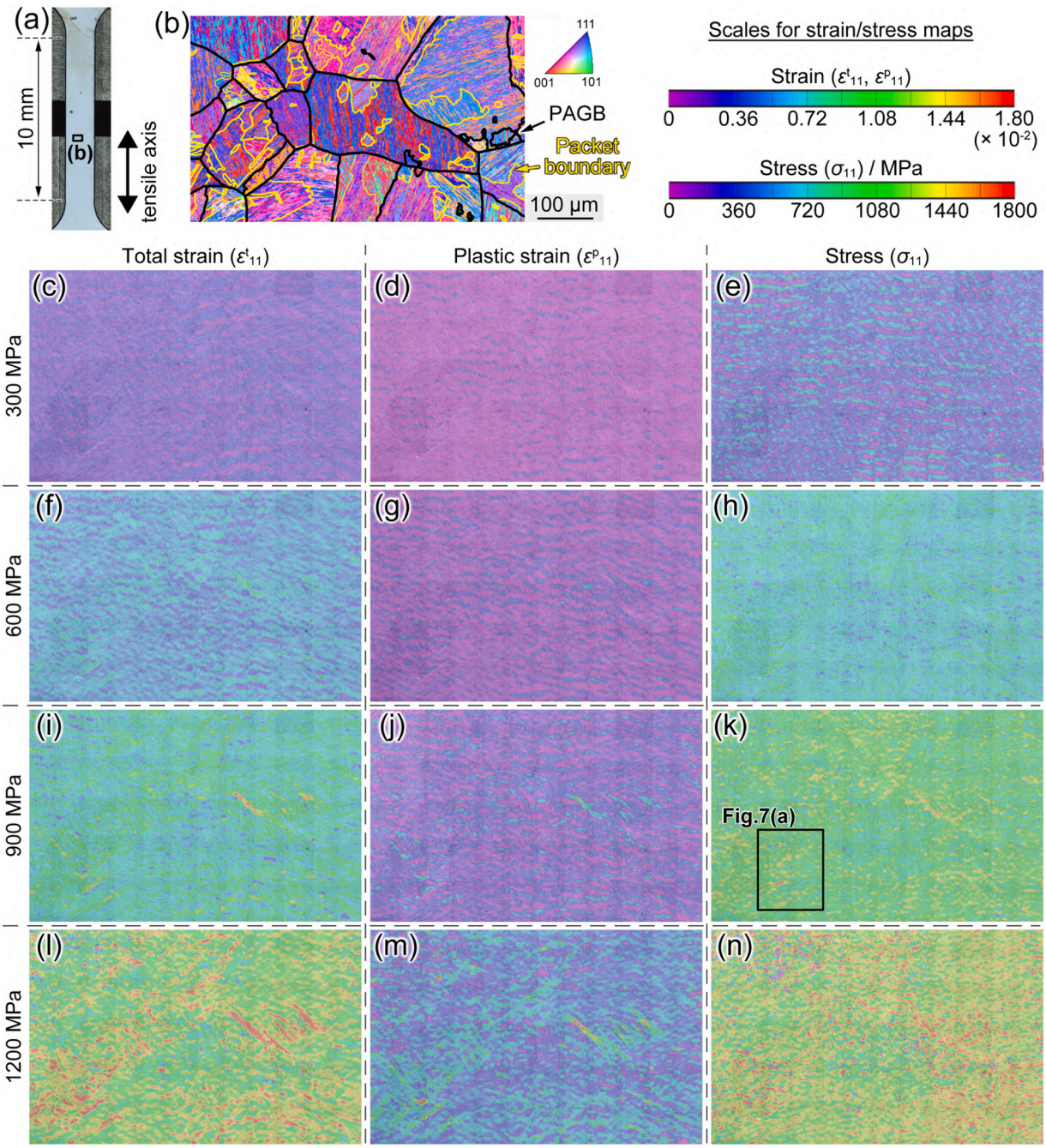

Fig. 3. Stress/strain distribution maps obtained by the advanced DIC analysis using microstructure-based patterns in the uncharged 0.2C_183μm specimen. (a) Optical microscopy image of the entire gauge part of the tensile specimen, (b) EBSD orientation map corresponding to the black rectangle in (a), distribution maps of (c, f, i, l) total strain (ε^t_{11}), (d, g, j, m) plastic strain (ε^p_{11}), and (e, h, k, n) stress (σ_{11}) in the tensile direction corresponding to (b); (c, d, e), (f, g, h), (i, j, k), and (l, m, n) show the maps at the nominal stress of 300, 600, 900, and 1200 MPa, respectively. PAGBs and packet boundaries are indicated by black and yellow lines, respectively, in (b).

improve the hydrophilicity of the sample surface, Ar ion milling (3 kV, 10 min) and plasma ion cleaning (40 W, 10 min) were performed. Following this, a colloidal silica suspension was promptly applied to the specimen surfaces, dried, and then the solute of the suspension was washed off by water. In the case of the silica pattern, contamination during observation and the resultant contrast changes in the SE images were significant, adversely affecting the recognition of random patterns in the DIC analysis. To mitigate the contamination, an osmium coating with a ~5 nm thickness was applied over the silica pattern. The tensile deformations were applied at constant displacements corresponding to nominal stress levels of 0, 300, 500, 650, 800, 900, 1000, 1100, and 1200 MPa. After confirming the saturation of stress relaxation at each holding stage, the SE and BSE images were simultaneously captured at an acceleration voltage of 20 kV and a current of 600 pA. The purpose of these SEM observation conditions is to achieve both the absence of microstructure contrast in SE images and the clear microstructure contrast in BSE images. The entire areas corresponding to the EBSD orientation maps were observed by capturing six SE images in the 0.1C_65μm and 0.2C_62μm specimens, or twenty-five SE images in the 0.1C_183μm specimen. Each of the SE images has a size of 160 × 120 μm and a resolution of 2560 × 1920 pixels. The subset and step sizes of the DIC analyses were 71 and 7 pixels, respectively, with 1 μm

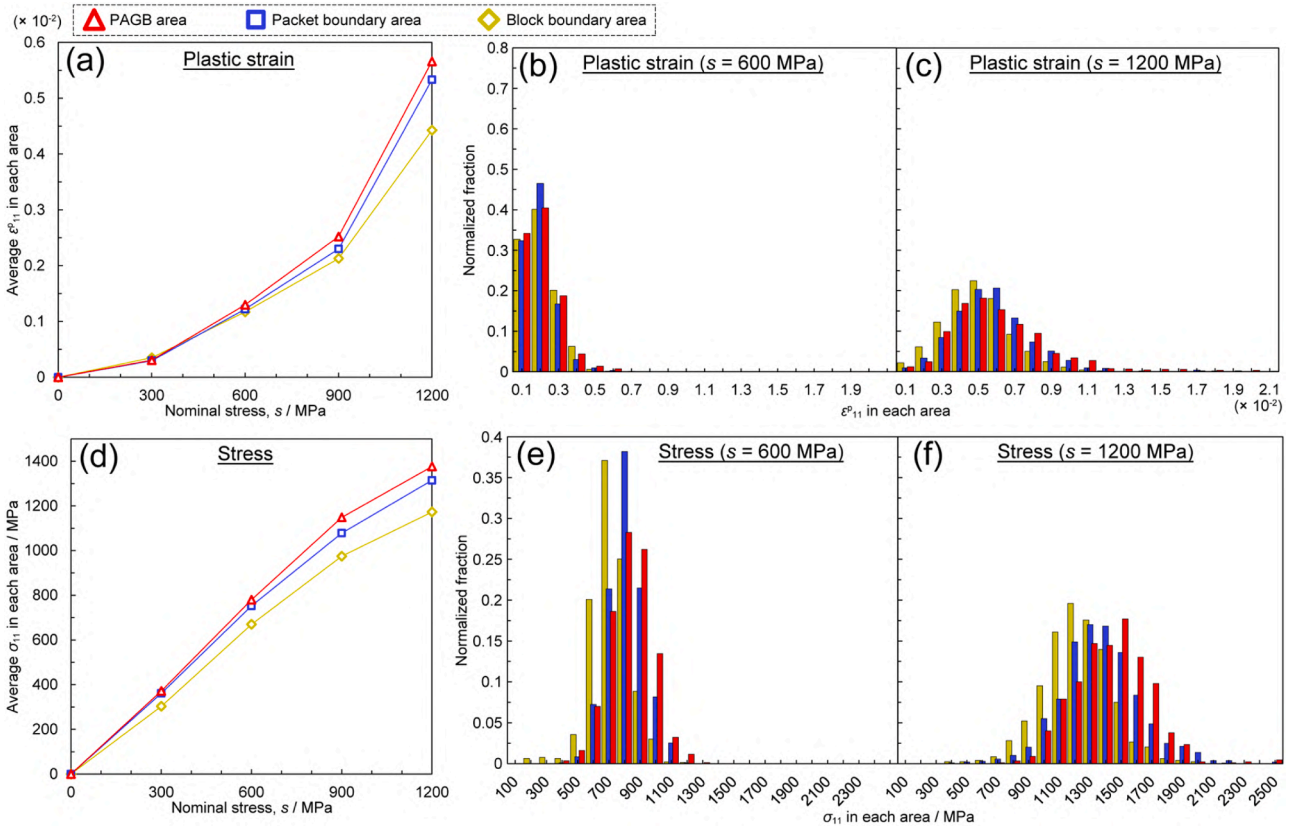

Fig. 4. Stress/strain partitioning behaviors corresponding to the martensitic structures. (a, d) Average ε^{p}_{11} and σ_{11}, respectively, as a function of nominal stress (s) within the PAGB (red), packet boundary (blue), and block boundary (dark yellow) areas. Stress/strain distribution histograms normalized for each area: (b) ε^{p}_{11} at the s of 600 MPa, (c) ε^{p}_{11} at the s of 1200 MPa, (e) σ_{11} at the s of 600 MPa, and (f) σ_{11} at the s of 1200 MPa.

corresponding to 16 pixels, which was the same as the microstructure-based DIC analysis. Fig. 1(d–f) shows an example of the 0.1C_65μm specimen at 0 MPa: **(d)** montages of six SE images and **(e)** montages of BSE images corresponding to **(d)**, and **(f)** an enlarged SE image of **(d)** showing the silica pattern. In the SE images (Fig. 1(d)), no contrast related to the microstructure is observed, making them suitable for comparing the DIC results with other martensitic steels. In the BSE images (Fig. 1(e)), the contrast corresponding to the martensitic microstructure is visible, enabling the identification of PAGB positions by comparing them with the EBSD orientation map.

3. Results

3.1. Hydrogen embrittlement behavior

Fig. 2(a–c) shows optical microscopy images of three as-quenched martensitic steels: **(a)** 3Mn-0.1C (wt. %) steel with a PAG size of 65 μm (referred to as "0.1C_65μm specimen") and **(b, c)** 3Mn-0.2C (wt. %) steels with PAG sizes of 62 and 183 μm (referred to as "0.2C_62μm" and "0.2C_183μm specimens"), respectively. The *TS* was 1.25, 1.65, and 1.50 GPa in the uncharged 0.1C_65μm, 0.2C_62μm, and 0.2C_183μm specimens, respectively. The nominal stress–nominal strain curves are shown in **Fig. S2(b–d)**. Fig. 2(d) summarizes the maximum stresses of the hydrogen-charged specimens normalized by the *TS* of the uncharged specimens (s_{max_norm}) as a function of the H_D. In the 0.2C_62μm and 0.2C_183μm specimens, the s_{max_norm} decreased with increasing the H_D and reached lower limits at certain H_D values (1 ~ 2 wt. ppm). The lower limit of s_{max_norm} was 0.32 (corresponding to the s_{max} of ~480 MPa) in the 0.2C_183μm specimen, much smaller than that in the 0.2C_62μm specimen (s_{max_norm} = 0.67). In contrast, the 0.1C_65μm was not embrittled by hydrogen (s_{max_norm} = 1) even when the H_D was as high as ~2.7 wt. ppm. We obtained three martensitic steels with different hydrogen embrittlement behaviors: severe, medium, and no embrittlement in the 0.2C_183μm, 0.2C_62μm, and 0.1C_65μm specimens, respectively.

Fig. 2(e) shows an SEM image of the fracture surface in the hydrogen-charged 0.2C_183μm specimen with the maximum H_D. Most of the fracture surface was covered by intergranular fracture surface. We confirmed that all the hydrogen-charged 0.2C_183μm and 0.2C_62μm specimens, whose s_{max_norm} was reduced by hydrogen, mainly fractured in an intergranular manner. In the 0.1C_65μm specimen, the fracture surface was mainly covered by ductile fracture surface with dimple patterns. Accordingly, we can discuss the resistance against the hydrogen-induced intergranular fracture by comparing the present three martensitic steels.

3.2. Stress/strain distribution corresponding to substructure boundaries

Fig. 3 shows the results of the advanced DIC analysis using microstructure-based patterns in the uncharged 0.2C_183μm specimen: **(a)** optical microscopy image of the entire gauge part of the tensile specimen, **(b)** EBSD orientation map corresponding to the black rectangle in **(a)**, distribution maps of **(c, f, i, l)** total strain (ε^{t}_{11}), **(d, g, j, m)** plastic strain (ε^{p}_{11}), and **(e, h, k, n)** stress (σ_{11}) in the tensile direction of the region corresponding to **(b); (c, d, e), (f, g, h), (i, j, k)**, and **(l, m, n)** show the maps at the nominal stress (s) of 300, 600, 900, and 1200 MPa, respectively. The PAGBs and packet boundaries are indicated by black and yellow lines, respectively. The stress/strain is distributed inhomogeneously and increases with the s. Especially at 600 and 900 MPa, which are below the 0.2 % proof stress (1058 MPa), the regions with high ε^{t}_{11} and σ_{11} correspond to the PAGBs of the large PAG in the center position (Fig. 3(f, h, i, k)), while plastic deformation is minimal (Fig. 3(g,

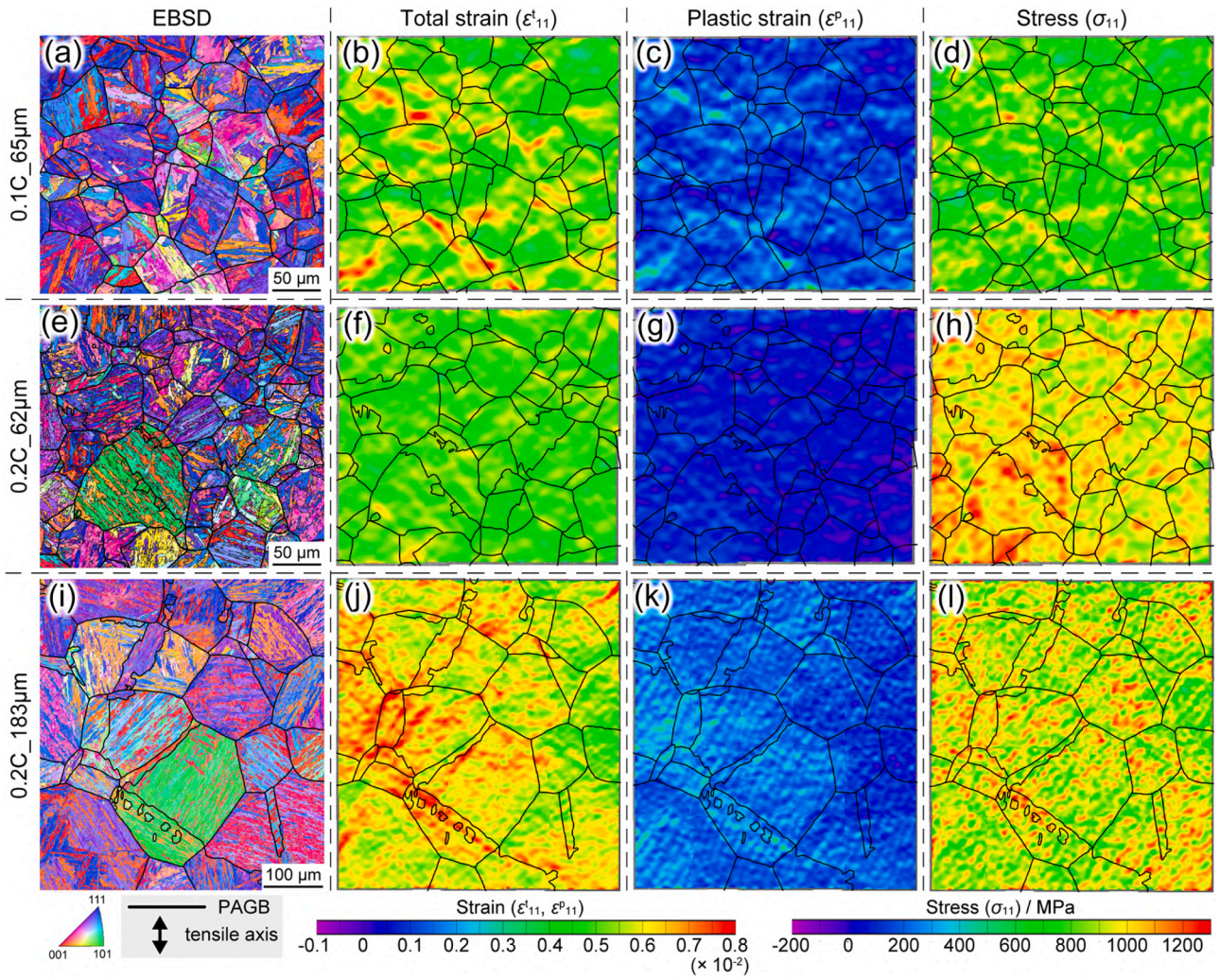

Fig. 5. Stress/strain distribution maps obtained by the advanced DIC analysis using silica patterns in the three martensitic steels. (a, e, i) EBSD orientation maps, corresponding (b, f, j) ε^t_{11} maps, (c, g, k) ε^p_{11} maps, and (d, h, l) σ_{11} maps: (a–d) 0.1C_65μm, (e–h) 0.2C_62μm, and (i–l) 0.2C_183μm specimens at the *s* of 1000 MPa. PAGBs are indicated by black lines.

j)). **Fig. S3** shows the true stress–true strain curve (blue) and the average σ_{11}–average ε^t_{11} curve of the entire observation area obtained by DIC analysis (red). The close match between these curves suggests that the stress values obtained by the present DIC analysis are reliable. To quantitatively correlate the stress/strain concentrations with substructure boundaries, the entire observation area was classified into three areas, i.e., PAGB, packet boundary, and block boundary areas. As shown in **Fig. S4**, the entire observation area was divided into 2.5 μm square domains, and the domains within the third nearest neighbors from the PAGBs were classified as the PAGB area. Next, among the remaining domains other than the PAGB area, those within the third nearest neighbors from the packet boundaries were classified as the packet boundary area. Finally, any undefined domains within the third nearest neighbors from the block boundaries were classified as the block boundary area. As a result, all domains were classified into one of these areas. The fractions of PAGB, packet boundary, and block boundary areas were 25.8, 31.6, and 42.6 %, respectively. Fig. 4(a, d) shows the average ε^p_{11} and σ_{11} within each area as a function of the *s*; red, blue, and yellow indicate the PAGB, packet boundary, and block boundary areas, respectively. At the *s* of 600 MPa or below, the ε^p_{11} in all areas was nearly the same. In contrast, the σ_{11} was the highest in the PAGB area, followed by the packet boundary area, and the lowest in the block boundary area. At the *s* of 900 MPa or above, both the ε^p_{11} and σ_{11} were the highest in the PAGB area, with the difference among the three areas increasing with the *s*. The stress/strain partitioning behavior is more evident in the stress/strain distribution histograms (Fig. 4(b, c, e, f)), in which the normalized fraction for each area is presented: **(b)** ε^p_{11} at the *s* of 600 MPa, **(c)** ε^p_{11} at the *s* of 1200 MPa, **(e)** σ_{11} at the *s* of 600 MPa, and **(f)** σ_{11} at the *s* of 1200 MPa. At the *s* of 600 MPa, the histograms of the ε^p_{11} were nearly the same in all areas, while those of the σ_{11} exhibited stress partitioning, i.e., highest in the PAGB area, followed by the packet, and then block boundary areas. For both the ε^p_{11} and σ_{11}, the distributions broadened, and the partitioning behavior was pronounced with the increase in the *s*. Since the hydrogen-charged 0.2C_183μm specimen fractured at a *s* of ~480 MPa (**Fig. S2(d)**), we conclude that local stress concentration at PAGBs, rather than plastic strain, plays a dominant role in the hydrogen-induced intergranular fracture. The histograms at all the nominal stress levels are shown in **Fig. S5**.

3.3. *Quantitative comparison between three martensitic steels*

Fig. 5 shows the results of the advanced DIC analysis using silica patterns in the uncharged **(a–d)** 0.1C_65μm, **(e–h)** 0.2C_62μm, and **(i–l)** 0.2C_183μm specimens at the *s* of 1000 MPa: **(a, e, i)** EBSD orientation maps with PAGBs indicated by the black lines, corresponding **(b, f, j)** ε^t_{11} maps, **(c, g, k)** ε^p_{11} maps, and **(d, h, l)** σ_{11} maps. The stress/strain maps at all stress levels are depicted in **Figs. S6–8** for the 0.1C_65μm, 0.2C_62μm, and 0.2C_183μm specimens, respectively. Compared with

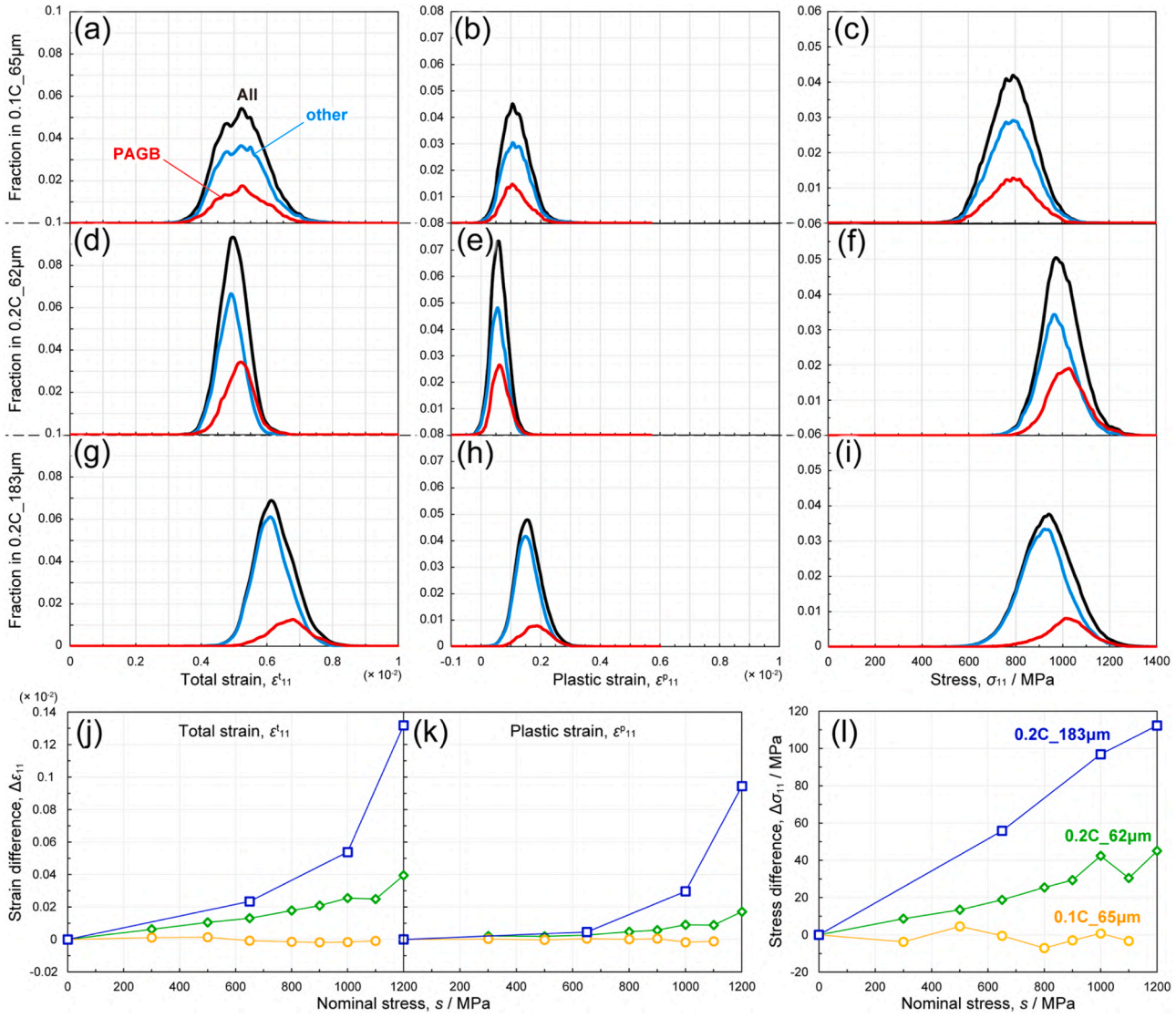

Fig. 6. Stress/strain concentration behaviors at PAGBs in the three martensitic steels. (a–i) Stress/strain distribution profiles corresponding to Fig. 5(b–d, f–h. and j–l), respectively. The profiles for all analyzed areas (black) are decomposed into the PAGB areas (red) and other areas (blue). (j–l) Differences in average stress/strain between the PAGB areas and the other areas as a function of the *s*: (j) total strain ($\Delta\varepsilon^t_{11}$), (k) plastic strain ($\Delta\varepsilon^p_{11}$), and (l) stress ($\Delta\sigma_{11}$).

the 0.1C_65μm specimen, the 0.2C_62μm specimen exhibits the stress/strain concentration areas more closely correlated with the PAGBs. The correspondence between the stress/strain concentration areas and PAGBs is much more pronounced in the 0.2C_183μm specimen. To quantitatively compare the stress/strain concentration at PAGBs, the areas within 4.5 μm from the PAGBs were classified as PAGB areas. We note that the definition of PAGB area is a bit different between the DIC analyses using microstructure and silica patterns due to technical issues, but there was no significant difference in the PAGB areas under both definitions. Fig. 6(a–i) shows the stress/strain distribution profiles corresponding to Fig. 5(b–d, f–h. and j–l), respectively. The stress/strain distribution profiles for all analyzed areas (black) are decomposed into the PAGB areas (red) and other areas (blue). There are 546,000 data points in the 0.1C_65μm and 0.2C_62μm specimens and 1,460,160 points in the 0.2C_183μm specimen. The fractions of PAGB areas were 29.8, 36.4, and 18.6 % in the 0.1C_65μm, 0.2C_62μm, and 0.2C_183μm specimens, respectively. The stress/strain partitioning was minimal in the 0.1C_65μm specimen, while it was evident in the 0.2C_62μm specimen and more pronounced in the 0.2C_183μm specimen. Fig. 6(j–l) shows the differences in average stress/strain between the PAGB areas and the other areas as a function of nominal stress: differences in **(j)** total strain ($\Delta\varepsilon^t_{11}$), **(k)** plastic strain ($\Delta\varepsilon^p_{11}$), and **(l)** stress ($\Delta\sigma_{11}$). The $\Delta\varepsilon^p_{11}$ was minimal below the *s* of 650 MPa in all the specimens, while the $\Delta\sigma_{11}$ linearly increased with the *s* in the 0.2C_62μm and 0.2C_183μm specimens. These results align with the microstructure pattern-based DIC analysis (**Figs.3, 4**, and **S5**). In addition, specimens with higher susceptibility to hydrogen embrittlement exhibited larger $\Delta\sigma_{11}$. This demonstrates that local stress concentration behavior at PAGBs is one of the most significant factors for hydrogen embrittlement susceptibility. The stress/strain distribution profiles at all nominal stress levels are shown in **Figs.S9–11** for the 0.1C_65μm, 0.2C_62μm, and 0.2C_183μm specimens, respectively.

4. Discussion

Generally, as-quenched martensitic steels exhibit high strength, but their elastic limits are notably low (~300 MPa) [47,48]. Plastic deformation at low stress levels would be attributed to the pre-existing dislocations introduced during martensitic transformation [48] and elastic anisotropy [49,50]. The hydrogen-charged 0.2C_183μm specimens fractured at the *s* of ~480 MPa, well above the elastic limit. Thus, hydrogen-induced intergranular fracture occurred after a certain degree

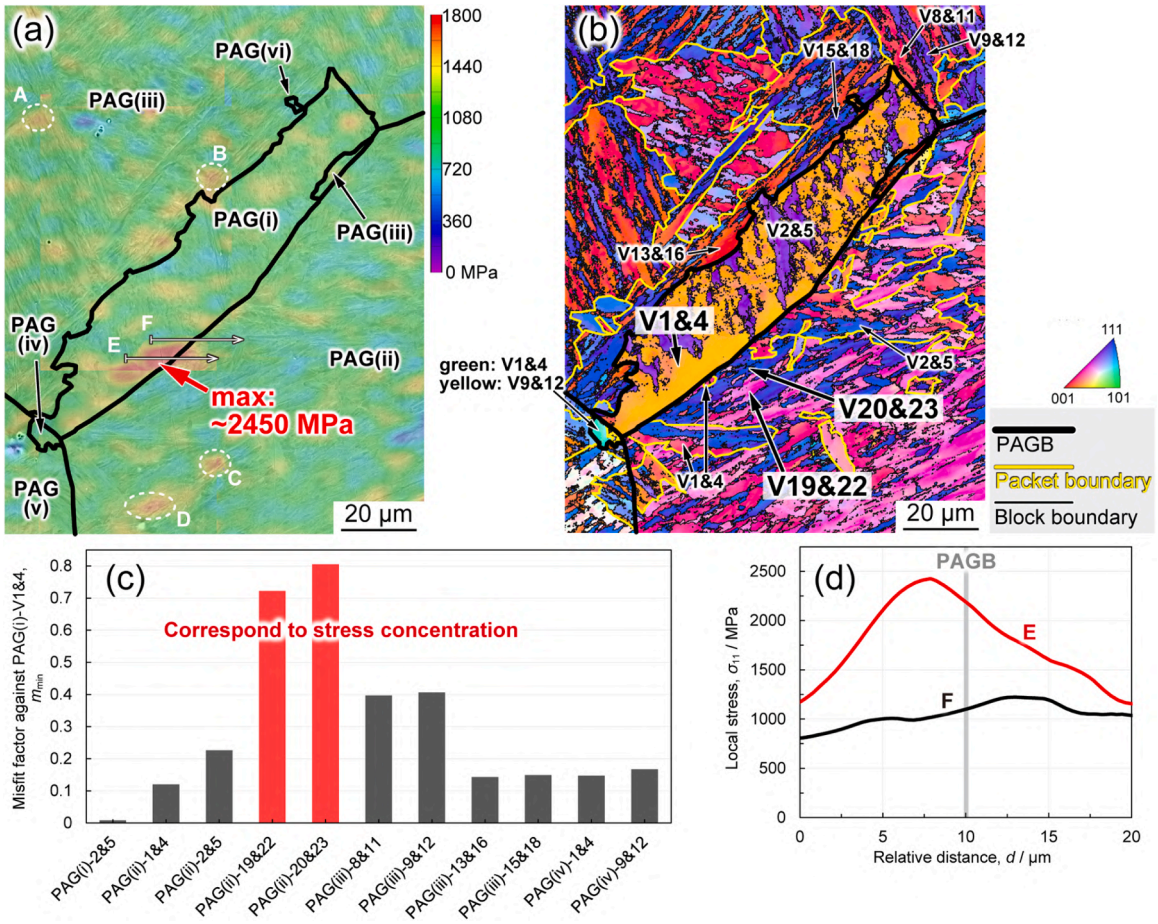

Fig. 7. Stress concentration behavior explained by the difficulty of slip transfer at PAGBs. (a) Enlarged stress distribution map corresponding to the black rectangle in Fig. 3(k). White broken circles (A–D) indicate the positions of stress concentrated areas at PAG interior. (b) EBSD orientation map corresponding to (a). PAGBs and packet boundaries are indicated by black and yellow lines, respectively. (c) Minimum misfit factor (m_{min}) at the boundaries between the V1&4 in PAG(i) and all the eleven adjacent variants. The variant boundaries (PAGBs) corresponding to the high-stress concentration site are indicated in red. (d) Spatial distribution profiles of local stress along the white arrows (E and F) crossing PAGB segments in (a).

of (local) plastic deformation. The present DIC results also demonstrate a certain degree of plastic deformation at low stress levels (Figs. 3–6 and **S5–11**). When a GB acts as an impenetrable boundary that does not allow shear to be transferred to the neighboring grain, i.e., slip transfer is difficult, dislocation pileup leads to local stress concentration at the GB [51,52]—namely, the lower the local plastic relaxation ability, the greater the local stress concentration at GBs. Soer and Hosson [52] proposed the following misfit factor (m), ranging from 0 (easy) to 1 (difficult), to evaluate the difficulty of slip transfer at GBs.

$$m = \sin\alpha \cdot \sin\beta \tag{2}$$

where α is the angle between the primary slip planes of adjacent grains, and β is the angle between the primary slip directions of adjacent grains. In martensitic steel, the slip system parallel to the lath (habit) plane (in-lath-plane slip system) is preferentially activated at small strain regimes (below 8 %) [53,54]. In this study, the following minimum misfit factor (m_{min}) is introduced to apply the misfit factor to martensitic steel without restricting the loading direction.

$$m_{min} = \sin\theta_{lath} \cdot \sin\varphi_{min} \tag{3}$$

where θ_{lath} is the angle between the habit planes of adjacent variants, and φ_{min} is the minimum value among the four angles between the in-lath-plane slip directions of adjacent variants. The lath plane is approximately parallel to the {011} plane and, concerning the {011} <111> slip system, each of the variants has two in-lath-plane slip directions.

Fig. 7(a) is an enlarged stress distribution map corresponding to the black rectangle in Fig. 3(k). Fig. 7(b) is an EBSD orientation map corresponding to **(a)**. PAGBs and packet boundaries are indicated by black and yellow lines, respectively. As indicated by the red arrow in Fig. 7(a), the maximum local stress of ~2450 MPa was concentrated around the PAGB even at the *s* of 900 MPa. The large stress concentration occurred at V1&4 in PAG(i), adjacent to the mixed region of V19&22 and V20&23 in PAG(ii). The m_{min} against the V1&4 in PAG(i) was calculated for all the eleven variants that exist adjacent to the V1&4 in PAG(i), shown in Fig. 7(c). As indicated in red, the two boundaries with particularly large m_{min} (V19&22 and V20&23 in PAG(ii) against V1&4 in PAG(i)) coincided exactly with the PAGB where significant local stress concentration occurred. As indicated by white broken circles (A–D) in Fig. 7(a), significant stress concentrations—reaching 1500~1800 MPa—also occur at packet boundaries. These packet boundaries also exhibit large m_{min}: A: 0.677, B: 0.735, C: 0.663, and D: 0.623. We emphasize that, while not all boundaries with large m_{min} necessarily show large stress concentrations, those boundaries that do exhibit large stress concentrations tend to have large m_{min}. The results demonstrated that the m_{min} is a valid indicator for assessing the susceptibility of stress concentration at boundaries. Fig. 7(d) is the spatial distribution profiles of local stress along the white arrows (E and F) crossing PAGB segments in **(a)**. The peak stress position does not perfectly coincide with the PAGB: ~2.5 μm away from the PAGB. This may have been influenced by factors such as the size and three-dimensional morphology of the variants adjacent to

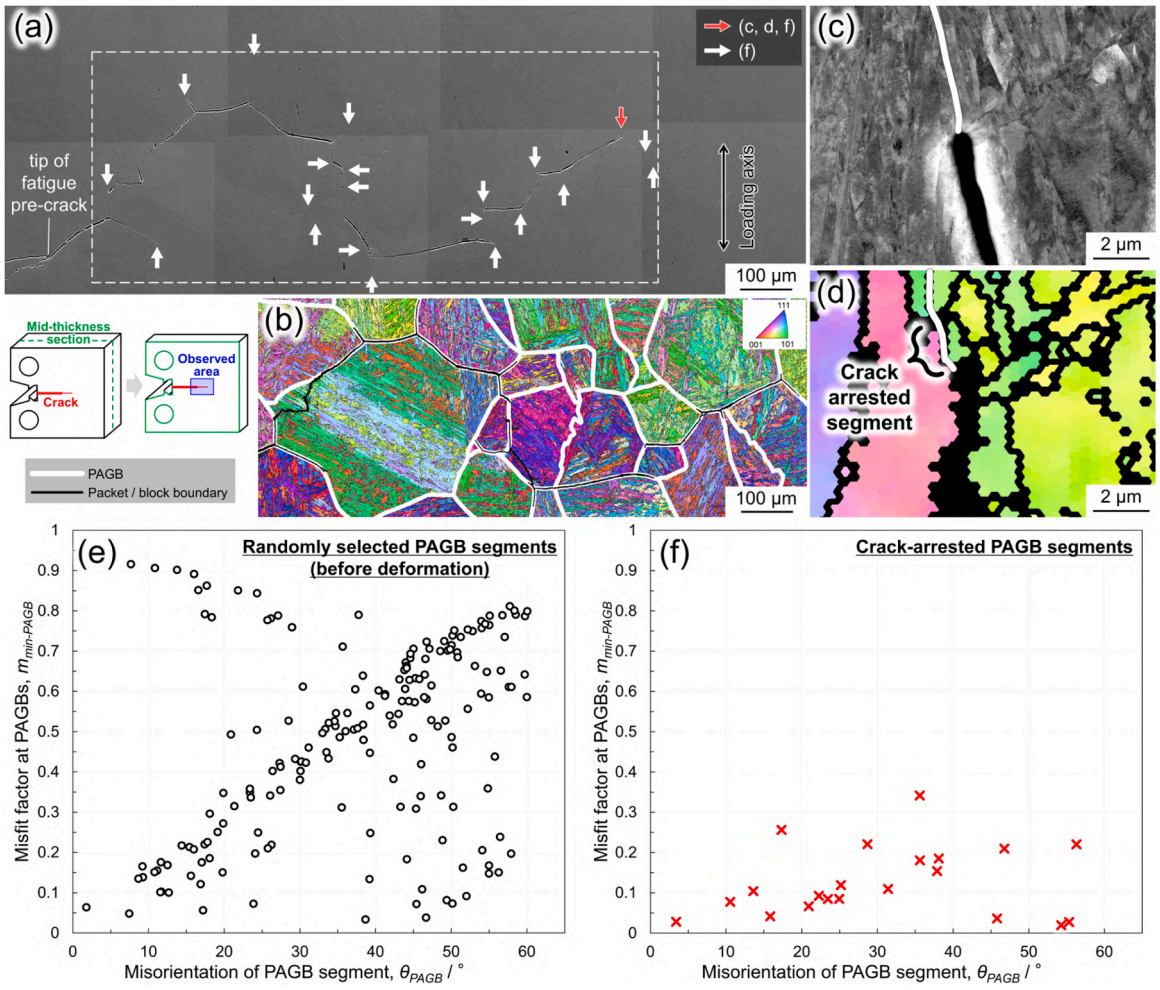

Fig. 8. Intergranular crack arrest behavior explained by the difficulty of slip transfer at PAGBs. (a) SE image at a region around the main crack in the hydrogen-charged 0.2C_183μm specimen (0.005 A m^{-2}) after the unloading compliance test stopped at $\Delta a \sim 0.8$ mm. (b) EBSD orientation map corresponding to the white broken rectangle in (a). (a) and (b) are cited from our previous work [28]. (c) Enlarged BSE image and (d) corresponding EBSD orientation map at a region indicated by a red arrow in (a). Relationships between misorientation (θ_{PAGB}) and misfit factor (m_{min_PAGB}) at (e) randomly selected PAGB segments before deformation or (f) crack-arrested PAGB segments. Twenty-one data points in (f) correspond to the arrested intergranular crack indicated by red or white arrows in (a).

the PAGBs (such as the inclination of the boundary in depth direction). In addition, Park et al. [45] also measured stress distributions using DIC analysis and reported that, although the peak position of σ_{11} is shifted by a few micrometers from the GB, the peak position of the von Mises equivalent stress coincides with the GB. The present study focuses on σ_{11}, rather than the von Mises equivalent stress, as the driving force for intergranular fracture, which is a kind of mode I fracture. In the present study, since the region within 4.5 μm from the PAGBs was defined as the PAGB area, the peak stresses were extracted as stresses within the PAGB area and plotted in Figs. 4 and 6.

To correlate the intergranular crack arrestability and local plastic relaxation ability, the unloading compliance tests at a current density of 0.005 A m^{-2} were stopped at a crack extension (Δa) of ~ 0.8 mm, and the mid-thickness section of the tested 0.2C_183μm specimen was observed. Details of the unloading compliance tests can be found in our previous work [28]. Fig. 8(a) is an SE image of a region around the main crack. As shown in the EBSD orientation map (Fig. 8(b)) corresponding to the white broken rectangle in **(a)**, the hydrogen-induced crack mainly propagated along PAGBs. As indicated by red or white arrows in Fig. 8 (a), twenty-one intergranular crack-tips—which microscopically arrested on the observed cross-section—were observed and one of them (red arrow) is enlarged in the **(c)** BSE image and **(d)** corresponding EBSD orientation map. The intergranular crack was arrested at a specific PAGB segment. Relationships between misorientation (θ_{PAGB}) and misfit factor (m_{min_PAGB}) at these crack-arrested PAGB segments are shown in Fig. 8 (f). The θ_{PAGB} and m_{min_PAGB} at the randomly selected PAGB segments before deformation (184 data points) are also shown in Fig. 8(e); the m_{min_PAGB} basically increases with the θ_{PAGB} up to ~ 0.8 with some exceptions. In contrast, almost all the m_{min_PAGB} at the crack-arrested PAGB segments are below ~0.25 even when the θ_{PAGB} is large. The results demonstrate that the local plastic relaxation ability is a key factor for the resistance against hydrogen-induced intergranular crack propagation. Shibata et al. [17,55] reported that the PAGB segments with small θ_{PAGB} locally arrested hydrogen-induced intergranular cracks; according to the present results, this would be due to the basically small m_{min_PAGB} at the PAGB segments with small θ_{PAGB}. In addition, even the PAGB segments with large θ_{PAGB} also arrest hydrogen-induced intergranular crack propagation when the m_{min_PAGB} is small. Therefore, the local plastic relaxation ability and resultant local stress concentration behavior control the hydrogen embrittlement resistance.

According to the K-S orientation relationship, the m_{min} of the twenty-three variant boundaries within a PAG (V2~V24 against V1) were calculated and summarized in Table 1. Since adjacent variants share the habit plane at block boundaries (V2~V6 against V1), the θ_{lath} is 0°, and m_{min} is 0. This suggests that slip transfer and the resultant local plastic relaxation are easy at block boundaries, making stress concentration less likely to occur. The θ_{lath} is always 70.53° at packet boundaries (V7~V24 against V1). However, for V7 and V8, one of their in-lath-plane slip

Table 1
m_{min} of the twenty-three variant boundaries within a PAG (V2∼V24 against V1).

Variant no.	Habit plane angle (θ_{lath})	Minimum slip direction angle (φ_{min})	Misfit factor (m_{min})
2	0°	0°	0
3	0°	10.53°	0
4	0°	10.53°	0
5	0°	10.53°	0
6	0°	21.06°	0
7	70.53°	0°	0
8	70.53°	0°	0
9	70.53°	49.47°	0.717
10	70.53°	10.53°	0.172
11	70.53°	10.53°	0.172
12	70.53°	49.47°	0.717
13	70.53°	10.53°	0.172
14	70.53°	10.53°	0.172
15	70.53°	53.66°	0.759
16	70.53°	17.16°	0.278
17	70.53°	12.11°	0.198
18	70.53°	46.75°	0.687
19	70.53°	49.47°	0.717
20	70.53°	49.47°	0.717
21	70.53°	52.06°	0.744
22	70.53°	46.75°	0.687
23	70.53°	53.66°	0.759
24	70.53°	57.02°	0.791

directions is parallel to those of V1 as shown in Fig. 9(a). Assuming the habit plane of V1 as $(011)_{V1}$ plane, the in-lath-plane slip directions are $[1\text{–}11]_{V1}$ and $[-1\text{–}11]_{V1}$. For V7, the in-lath plane slip direction $[11\text{–}1]_{V7}$ on $(011)_{V7}$ habit plane is parallel to the $[-1\text{–}11]_{V1}$ direction, and, for V8, the $[1\text{–}11]_{V8}$ direction is also parallel to the $[-1\text{–}11]_{V1}$ direction. As a result, at the V1-V7 and V1-V8 packet boundaries, the φ_{min} (and m_{min}) is 0, indicating that slip transfer (local plastic relaxation) can easily occur. According to the misorientation angle and axis at the twenty-three variant boundaries in the K-S orientation relationship [56, 57], the length fraction of each variant boundary was measured using the EBSD orientation maps and summarized in Fig. 9(b). Most variant boundaries are block boundaries, and a large fraction of the packet boundaries are V1-V7 and V1-V8 boundaries, where the m_{min} is 0. Large fractions of V1-V8 packet boundaries were also reported by Stormvinter et al. [56] in Fe-C binary alloys. Fig. 9(c) shows the histograms of the m_{min} at packet boundaries (m_{min_packet}) weighted by the length fraction shown in **(b)**. A large fraction of the m_{min_packet} is 0 in all three martensitic steels, which is due to the large fraction of the V1-V7 and V1-V8 boundaries. The average m_{min_packet} ($m_{min\_packet.ave}$) was 0.338, 0.347, and 0.248 in the 0.1C_65μm, 0.2C_62μm, and 0.2C_183μm specimens, respectively. Fig. 9(d) shows the histograms of the m_{min_PAGB} weighted by their length fractions. The m_{min_PAGB} was calculated for approximately 200 randomly selected PAGB segments for each specimen; for the 0.2C_183μm specimen, data corresponds to Fig. 8(e). The m_{min_PAGB} is distributed randomly compared to the m_{min_packet}. The average m_{min_PAGB} ($m_{min\_PAGB.ave}$) was 0.286, 0.472, and 0.586 in the 0.1C_65μm, 0.2C_62μm, and 0.2C_183μm specimens, respectively. When the m_{min} of PAGBs is larger than that of packet boundaries, slip transfer (local plastic relaxation) is relatively difficult at PAGBs compared to within the PAGs, leading to stress concentration at PAGBs. Therefore, we introduced the "relative misfit factor at PAGB ($m_{min\_PAGB.ave}/m_{min\_packet.ave}$)" as an indicator of the relative difficulty of slip transfer at PAGBs against within PAGs. In other words, the $m_{min\_PAGB.ave}/m_{min\_packet.ave}$ larger than 1 indicates that local plastic relaxation is relatively difficult at the PAGBs. In the 0.1C_65μm specimen, the $m_{min\_PAGB.ave}/m_{min\_packet.ave}$ is 0.85, i.e., relatively easy relaxation, and the $\Delta\sigma_{11}$ is minimal. In the 0.2C_62μm ($m_{min\_PAGB.ave}/m_{min\_packet.ave}$ = 1.36) and 0.2C_183μm ($m_{min\_PAGB.ave}/m_{min\_packet.ave}$ = 2.36) specimens, significant stress concentration was observed at the PAGBs, and the $\Delta\sigma_{11}$ increased with the $m_{min\_PAGB.ave}/m_{min\_packet.ave}$ (Fig. 6(l)). As shown in Fig. 9, the differences in the $m_{min\_PAGB.ave}/m_{min\_packet.ave}$ values among three martensitic steels are determined by the types of variants adjacent to the PAGBs and the substructure boundaries within PAGs—namely, the variant selection behavior during the martensitic transformation.

In Fig. 10, the vertical axis shows the lower limit of the s_{max_norm} in the hydrogen-charged specimens; the smaller s_{max_norm} means severely embrittled. The horizontal and depth axes show the $\Delta\sigma_{11}$ at the s of 1000 MPa and the $m_{min\_PAGB.ave}/m_{min\_packet.ave}$, respectively. The result clearly demonstrates that, in the present three martensitic steels, as relative plastic relaxation at PAGBs becomes more difficult compared to within PAGs, the consequent stress concentration at PAGBs increases, leading to more severe hydrogen embrittlement (making intergranular fracture easily occur). Stress concentration not only serves as a driving force for PAGB decohesion, but also promotes hydrogen accumulation at PAGBs and facilitates the reduction of PAGB cohesive energy; namely, the local stress threshold required for PAGB decohesion is reduced. Hydrogen tends to accumulate in regions with high hydrostatic stress fields [56, 57]. Thus, we conclude that the preferential hydrogen accumulation and intergranular fracture at PAGBs are due to the relative difficulty of plastic relaxation at PAGBs against within PAGs and the resultant stress concentration at PAGBs. From the perspective of intergranular fracture, the origin of the susceptibility to hydrogen embrittlement is the local stress concentration related to the variant selection behavior at PAGBs in the martensitic transformation. In this study, the *TS* (ranging from 1.25 to 1.65 GPa) was controlled by changing carbon composition and austenitization temperature (and resultant PAG size), which are the most common dominant factors governing the *TS* of martensitic steels. The variant selection behavior itself is not as decisive a factor for *TS* as carbon composition; however, it is affected by chemical composition (such as carbon [58]), transformation temperature [59], and mechanical processing (such as ausforming [60]), etc. In the 0.1C_65μm and 0.2C_62μm specimens, the austenitization temperature was the same (900 °C) as well as the PAG size, and the hydrogen embrittlement resistance decreased with increasing the *TS*. These two specimens clearly show the trade-off relationship between the *TS* and hydrogen embrittlement resistance, which was affected by the carbon composition. The martensite start (*Ms*) temperature decreases with increasing the carbon composition [61], which may increase the hardness of the parent austenite matrix at the transformation temperature and change the resultant variant selection behavior. Carbon composition would be one of the origins of the trade-off. In contrast, the 0.2C_62μm and 0.2C_183μm specimens have the same chemical composition, while the PAG sizes are different, and the hydrogen embrittlement resistance increased with the *TS*. The result breaks the trade-off relationship, suggesting that the PAG size is another controlling factor for the variant selection behavior. The improved hydrogen-resistance by PAG refinement was also reported previously [57–63]. According to our results, these improvements can be attributed to the variant selection behavior, which is affected by the PAG size. The *Ms* temperature decreases with the PAG size. However, within the PAG size range of 50 ∼ 200 μm, the effect of PAG size on the *Ms* temperature is significantly smaller than that of carbon composition [64,65]. In this case, *Ms* temperature would not be the dominant factor for the variant selection. A deeper understanding of the variant selection behavior in martensitic transformation is demanded in the future. This study demonstrated both the origin of the trade-off (i.e., carbon composition) and a strategy for breaking the trade-off (i.e., PAG refinement), and both can be understood in terms of the shared factors: sensitivity to the intergranular fracture, strongly depending on the local stress concentration at PAGBs related to variant selection behavior in the martensitic transformation. We propose that controlling the variant selection behavior, the consequent relative difficulty of plastic relaxation at PAGBs against within PAGs, and local stress concentration behavior would be essential for designing hydrogen-resistant high-strength martensitic steels.

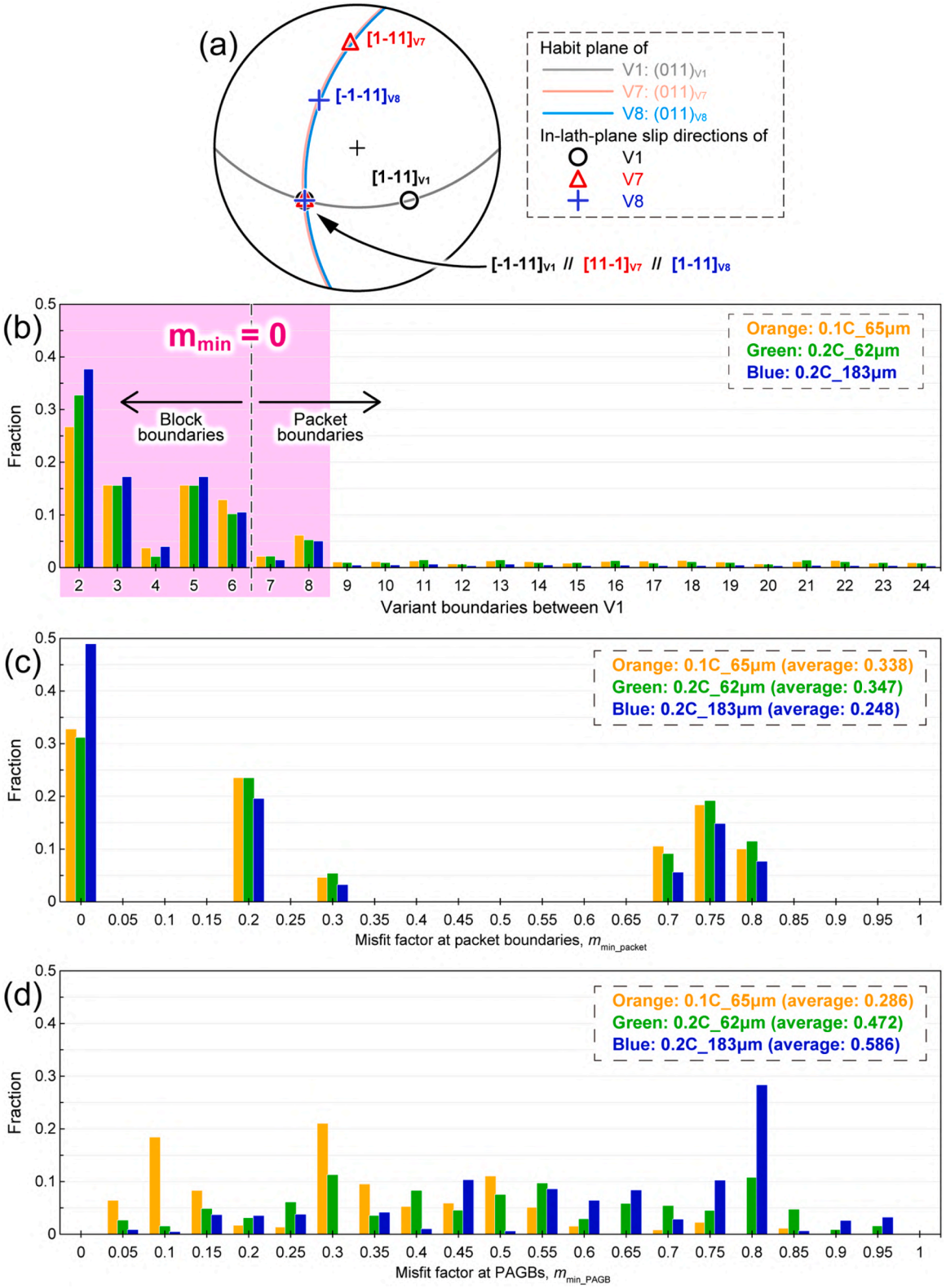

Fig. 9. Minimum misfit factors at variant/PAG boundaries. (a) Stereographic projection showing the habit planes and in-lath-plane slip directions in V1, V7, and V8. (b) Length fraction of each variant boundary. (c) Histograms of the m_{min} at packet boundaries (m_{min_packet}) weighted by the length fraction shown in (b). (d) Histograms of the m_{min} at PAGBs (m_{min_PAGB}) weighted by the length fraction.

5. Conclusion

This study clarified the origin of the trade-off relationship between the *TS* and hydrogen embrittlement resistance from a perspective of sensitivity to the hydrogen-induced intergranular fracture. The local stress concentration at PAGBs during uniaxial tensile deformation was quantitatively evaluated using the digital image correlation (DIC) method. Comparing three as-quenched martensitic steels with different

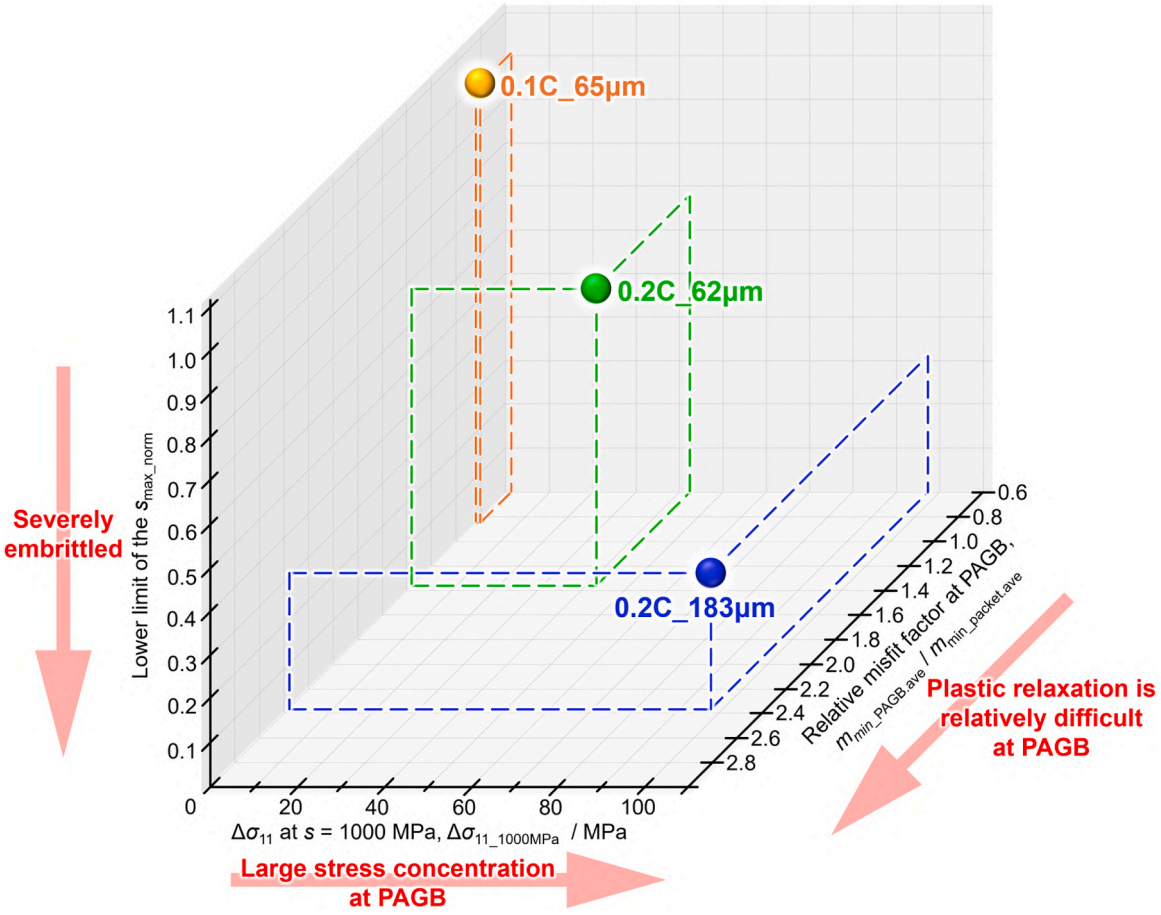

Fig. 10. Relationship between hydrogen embrittlement susceptibility, stress concentration behavior, and plastic relaxation ability of PAGB areas. The vertical, horizontal, and depth axes show the lower limit of the s_{max_norm} in the hydrogen-charged specimens, $\Delta\sigma_{11}$ at the s of 1000 MPa, and the $m_{min\_PAGB.ave}$/ $m_{min\_packet.ave}$, respectively.

TS and different resistance against hydrogen-induced intergranular fracture, the origin of the trade-off was revealed in terms of the variant selection behavior in martensitic transformation, the consequent relative difficulty of plastic relaxation at PAGBs against within PAGs, and local stress concentration behavior at PAGBs. The *TS*, ranging from 1.25 to 1.65 GPa, was controlled by changing carbon composition and austenitization temperature (and resultant PAG size). The major conclusions are as follows;

(1) Crystallographically, the local plastic relaxation capability of prior austenite grain boundaries (PAGBs) is relatively lower than that of other substructure boundaries (within PAGs). As a result, PAGBs experience higher local stress concentration compared to other substructure boundaries, leading to preferential hydrogen accumulation and intergranular cracking at PAGBs.
(2) As the relative difficulty of plastic relaxation at PAGBs compared to within PAGs increases, the consequent stress concentration at PAGBs increases, leading to more severe hydrogen embrittlement (making intergranular fracture easily occur).
(3) The origin of the trade-off between tensile strength and hydrogen resistance is the variant selection behavior in martensitic transformation, affected by carbon composition, and the resultant local plastic relaxation ability of the PAGB region. PAG refinement improves both tensile strength and hydrogen resistance, breaking the trade-off due to the change in variant selection behavior and the resultant suppression of stress concentration.

CRediT authorship contribution statement

Kazuho Okada: Writing – review & editing, Writing – original draft, Visualization, Validation, Project administration, Methodology, Investigation, Funding acquisition, Formal analysis, Data curation, Conceptualization. **Yukihisa Watase:** Writing – review & editing, Validation, Methodology, Investigation. **Myeong-heom Park:** Writing – review & editing, Validation, Methodology, Investigation, Formal analysis. **Kaneaki Tsuzaki:** Writing – review & editing, Methodology, Conceptualization. **Akinobu Shibata:** Writing – review & editing, Supervision, Resources, Project administration, Funding acquisition, Conceptualization.

Declaration of competing interest

The authors declare that they have no known competing financial interests or personal relationships that could have appeared to influence the work reported in this paper.

Acknowledgments

K.O. thanks the financial support from the Japan Society for the Promotion of Science (JSPS) KAKENHI grant (JP23K13541), the Iketani Science and Technology Foundation (0351190-A), and the Japan Science and Technology Agency ACT-X grant (JPMJAX23D5). A.S. was financially supported by the JSPS KAKENHI grant (JP23K26410).

Supplementary materials

Supplementary material associated with this article can be found, in the online version, at doi:10.1016/j.actamat.2025.121683.

References

[1] T. Fujita, Y. Yamada, Physical metallurgy and SCC in high strength steels, Stress Corros. Cracking Hydrogen Embrittlement Iron Base Alloys 5 (1977) 736. NACE.
[2] S. Lynch, Hydrogen embrittlement phenomena and mechanisms, Corros. Rev. 30 (2012) 105–1023.
[3] I.M. Robertson, P. Sofronis, A. Nagao, M.L. Martin, S. Wang, D.W. Gross, K. E. Nygren, Hydrogen embrittlement understood, Metall. Mater. Trans. B 46 (2015) 1085–1103.
[4] M. Dadfarnia, A. Nagao, S. Wang, M.L. Martin, B.P. Somerday, P. Sofronis, Recent advances on hydrogen embrittlement of structural materials, Int. J. Fracture 196 (2015) 223–243.
[5] J. Venezuela, Q. Liu, M. Zhang, Q. Zhou, A. Atrens, A review of hydrogen embrittlement of martensitic advanced high-strength steels, Corros. Rev. 34 (2016) 153–186.
[6] W. Zhong, Y. Cai, D. Tománek, Computer simulation of hydrogen embrittlement in metals, Nature 362 (1993) 435–437.
[7] D. Raabe, C.C. Tasan, E.A. Olivetti, Strategies for improving the sustainability of structural metals, Nature 575 (2019) 64–74.
[8] J. Song, W.A. Curtin, Atomic mechanism and prediction of hydrogen embrittlement in iron, Nat. Mater. 12 (2013) 145–151.
[9] Y. Hagihara, T. Shobu, N. Hisamori, H. Suzuki, K. Takai, K. Hirai, Delayed fracture using CSRT and hydrogen trapping characteristics of V-bearing high-strength steel, ISIJ Int; 52 (2012) 298–306.
[10] A.R. Marder, G. Krauss, The morphology of martensite in iron-carbon alloys, Trans. Am. Soc. Metals 60 (1967) 651–660.
[11] G. Krauss, A.R. Marder, The morphology of martensite in iron alloys, Metall. Transa 2 (1971) 2343–2357.
[12] S. Morito, H. Tanaka, R. Konishi, T. Furuhara, T. Maki, The morphology and crystallography of lath martensite in Fe-C alloys, Acta Mater. 51 (2003) 1789–1799.
[13] S. Morito, X. Huang, T. Furuhara, T. Maki, N. Hansen, The morphology and crystallography of lath martensite in alloy steels, Acta Mater. 54 (2006) 5323–5331.
[14] A. Shibata, G. Miyamoto, S. Morito, A. Nakamura, T. Moronaga, H. Kitano, I. G. Urrutia, T. Hara, K. Tsuzaki, Substructure and crystallography of lath martensite in as-quenched interstitial-free steel and low-carbon steel, Acta Mater. 246 (2023) e118675.
[15] M. Wang, E. Akiyama, K. Tsuzaki, Effect of hydrogen on the fracture behavior of high strength steel during slow strain rate test, Corros. Sci. 49 (2007) 4081–4097.
[16] A. Shibata, Y. Momotani, T. Murata, T. Matsuoka, M. Tsuboi, N. Tsuji, Microstructural and crystallographic features of hydrogen-related fracture in lath martensitic steels, Mater. Sci. Technol. 33 (2017) 1524–1532.
[17] A. Shibata, I.G. Urrutia, A. Nakamura, K. Okada, G. Miyamoto, Y. Madi, J. Besson, T. Hara, K. Tsuzaki, Three-dimensional propagation behavior of hydrogen-related intergranular cracks in high-strength martensitic steel, Int. J. Hydrogen Energy 48 (2023) 34565–34574.
[18] S.J. Lee, J.A. Ronevich, G. Krauss, D.K. Matlock, Hydrogen embrittlement of hardened low-carbon sheet steel, ISIJ Int. 50 (2010) 294–301.
[19] J. Ovejero-Garcia, Hydrogen microprint technique in the study of hydrogen in steels, J. Mater. Sci. 20 (1985) 2623–2629.
[20] K. Takai, J. Seki, Y. Homma, Observation of trapping sites of hydrogen and deuterium in high-strength steels by using secondary ion mass spectrometry, Mater. Trans. 36 (1995) 1134–1139.
[21] Y. Momotani, A. Shibata, D. Terada, N. Tsuji, Effect of strain rate on hydrogen embrittlement in low-carbon martensitic steel, Int. J. Hydrogen Energy 42 (2017) 3371–3379.
[22] Y. Momotani, A. Shibata, T. Yonemura, Y. Bai, N. Tsuji, Effect of initial dislocation density on hydrogen accumulation behavior in martensitic steel, Scr. Mater. 178 (2020) 318–323.
[23] M. Yamaguchi, J. Kameda, K. Ebihara, Mobile effect of hydrogen on intergranular decohesion of iron: first-principles calculations, Phil. Mag. 92 (2012) 1349–1368. Corrigendum 92 (2012), 3121–3124.
[24] S. Wang, M.L. Martin, I.M. Robertson, P. Sofronis, Effect of hydrogen environment on the separation of Fe grain boundaries, Acta Mater. 107 (2016) 279–288.
[25] S.P. Jung, Y. Kwon, C.S. Lee, B.J. Lee, Influence of hydrogen on the grain boundary crack propagation in bcc iron: a molecular dynamics simulation, Comput. Mater. Sci. 149 (2018) 424–434.
[26] K. Okada, A. Shibata, T. Sasaki, H. Matsumiya, K. Hono, N. Tsuji, Improvement of resistance against hydrogen embrittlement by controlling carbon segregation at prior austenite grain boundary in 3Mn-0.2C martensitic steels, Scr. Mater 224 (2023) e115043.
[27] M. Yamaguchi, J. Kameda, Intergranular decohesion induced by mobile hydrogen in iron with and without segregated carbon: first-principles calculations, in: International Hydrogen Conference (HIC 2012): Hydrogen-Materials Interactions, American Society of Mechanical Engineers (ASME) Press, 2014, pp. 747–755.
[28] K. Okada, A. Shibata, Y. Kimura, M. Yamaguchi, K. Ebihara, N. Tsuji, Effect of carbon segregation at prior austenite grain boundary on hydrogen-related crack propagation behavior in 3Mn-0.2C martensitic steels, Acta Mater. 224 (2024) 120288 e.
[29] A. Nagao, M.L. Martin, M. Dadfarnia, P. Sofronis, I.M. Robertson, The effect of nanosized (Ti,Mo)C precipitates on hydrogen embrittlement of tempered lath martensitic steel, Acta Mater. 74 (2014) 244–254.
[30] S. Zhang, J. Wan, Q. Zhao, J. Liu, F. Huang, Y. Huang, X. Li, Dual role of nanosized NbC precipitates in hydrogen embrittlement susceptibility of lath martensitic steel, Corros. Sci. 164 (2020) e108345.
[31] S. Zhang, D. Xu, F. Huang, W. Gao, J. Wan, J. Liu, Mitigation of hydrogen embrittlement in ultra-high strength lath martensitic steel via Ta microalloying, Mater. Des. 210 (2021) e110090.
[32] B. Zhang, Q. Zhu, C. Xu, C. Li, Y. Ma, Z. Ma, S. Liu, R. Shao, Y. Xu, B. Jiang, L. Gao, X. Pang, Y. He, G. Chen, L. Qiao, Atomic-scale insights on hydrogen trapping and exclusion at incoherent interfaces of nanoprecipitates in martensitic steels, Nat. Commun. 13 (2022) e3858.
[33] Y.S. Chen, D. Haley, S.S.A. Gerstl, A.J. London, F. Sweeney, R.A. Wepf, W. M. Rainforth, P.A.J. Bagot, M.P. Moody, Direct observation of individual hydrogen atoms at trapping sites in a ferritic steel, Science 355 (2017) 1196–1199.
[34] Y.S. Chen, H. Lu, J. Liang, A. Rosenthal, H. Liu, G. Sneddon, I. McCarroll, Z. Zhao, W. Li, A. Guo, J.M. Cairney, Observation of hydrogen trapping at dislocations, grain boundaries, and precipitates, Science 367 (2020) 171–175.
[35] P. Gong, J. Nutter, P.E.J. Rivera-Diaz-Del-Castillo, W.M. Rainforth, Hydrogen embrittlement through the formation of low-energy dislocation nanostructures in nanoprecipitation-strengthened steels, Sci. Adv. 6 (2020) eabb6152.
[36] B. Sun, W. Lu, B. Gault, R. Ding, S.K. Makineni, D. Wan, C.H. Wu, H. Chen, D. Ponge, D. Raabe, Chemical heterogeneity enhances hydrogen resistance in high-strength steels, Nat. Mater. 20 (2021) 1629–1634.
[37] M. Wang, E. Akiyama, K. Tsuzaki, Effect of hydrogen on the fracture behavior of high strength steel during slow strain rate test, Corros. Sci. 49 (2007) 4081–4097.
[38] M. Wang, E. Akiyama, K. Tsuzaki, Determination of the critical hydrogen concentration for delayed fracture of high strength steel by constant load test and numerical calculation, Corros. Sci. 48 (2006) 2189–2202.
[39] T.C. Chu, W.F. Ranson, M.A. Sutton, W.H. Peters, Applications of digital-image-correlation techniques to experimental mechanics, Exp. Mech. 25 (1985) 232–244.
[40] B. Wattrisse, A. Chrysochoos, J.M. Muracciole, M. Némoz-Gaillard, Analysis of strain localization during tensile tests by digital image correlation, Exp. Mech. 41 (2001) 29–39.
[41] F.D. Gioacchino, J.Q. Fonseca, Plastic strain mapping with sub-micron resolution using digital image correlation, Exp. Mech. 53 (2013) 743–754.
[42] A.J. Wilkinson, G. Meaden, D.J. Dingley, High-resolution elastic strain measurement from electron backscatter diffraction patterns: new levels of sensitivity, Ultramicroscopy 106 (2006) 307–313.
[43] A.J. Wilkinson, Methods for determining elastic strains from electron backscatter diffraction and electron channelling patterns, Mater. Sci. Technol. 13 (2012) 79–84.
[44] S. Yamasaki, H. Matsuo, T. Morikawa, M. Tanaka, Acquisition of microscopic and local stress-strain curves by combination of HR-EBSD and DIC methods, Scr. Mater. 235 (2023) e115603.
[45] M. Park, S. Yako, Y. Takeda, A. Shibata, N. Tsuji, Making stress visible: a method to quantify local stress distribution in metals using digital image correlation method, Scr. Mater. 252 (2024) e116265.
[46] D. Yan, C.C. Tasan, D. Raabe, High resolution in situ mapping of microstrain and microstructure evolution reveals damage resistance criteria in dual phase steels, Acta Mater. 96 (2015) 399–409.
[47] G. Krauss, Martensite in steel: strength and structure, Mater. Sci. Eng.: A (1999) 40–57, 273–275.
[48] S. Takaki, K.L. Ngo-Huynh, N. Nakada, T. Tsuchiyama, Strengthening mechanism in ultra low carbon martensitic steel, ISIJ Int. 52 (2012) 710–716.
[49] B. Clausen, T. Lorentzen, T. Leffers, Self-consistent modeling of the plastic deformation of f.c.c. polycrystals and its implications for diffraction measurements of internal stresses, Acta Mater. 46 (1998) 3087–3098.
[50] C.J. Neil, J.A. Wollmershauser, B. Clausen, C.N. Tomé, S.R. Agnew, Modeling lattice strain evolution at finite strains and experimental verification for copper and stainless steel using in situ neutron diffraction, Int. J. Plast. 26 (2010) 1772–1791.
[51] T.R. Bieler, P. Eisenlohr, C. Zhang, H.J. Phukan, M.A. Crimp, Grain boundaries and interfaces in slip transfer, Current Opinion Solid State Mater. Sci. 18 (2014) 212–226.
[52] W.A. Soer, J.Th.M. De Hosson, Detection of grain-boundary resistance to slip transfer using nanoindentation, Mater. Lett. 59 (2005) 3192–3195.
[53] S. Nambu, M. Michiuchi, Y. Ishimoto, K. Asakura, J. Inoue, T. Koseki, Transition in deformation behavior of martensitic steel during large deformation under uniaxial tensile loading, Scr. Mater. 60 (2009) 221–224.
[54] M. Michiuchi, S. Nambu, Y. Ishimoto, J. Inoue, T. Koseki, Relationship between local deformation behavior and crystallographic features of as-quenched lath martensite during uniaxial tensile deformation, Acta Mater. 57 (2009) 5283–5291.
[55] A. Shibata, I. Gutierrez-Urrutia, A. Nakamura, T. Moronaga, K. Okada, Y. Madi, J. Besson, T. Hara, Local crack arrestability and deformation microstructure evolution of hydrogen-related fracture in martensitic steel, Corros. Sci. 233 (2024) e112092.
[56] R. Kirchheim, Revisiting hydrogen embrittlement models and hydrogen-induced homogeneous nucleation of dislocations, Scr. Mater. 62 (2010) 67–70.
[57] L. Cho, P.E. Bradley, D.S. Lauria, M.J. Connolly, E.J. Seo, K.O. Findley, J.G. Speer, L. Golem, A.J. Slifka, Effects of hydrogen pressure and prior austenite grain size on the hydrogen embrittlement characteristics of a press-hardened martensitic steel, Int. J. Hydrogen Energy 46 (2021) 24425–24439.

[58] A. Stormvinter, G. Miyamoto, T. Furuhara, P. Hedström, A. Borgenstam, Effect of carbon content on variant pairing of martensite in Fe–C alloys, Acta Mater. 60 (2012) 7265–7274.
[59] N. Takayama, G. Miyamoto, T. Furuhara, Effects of transformation temperature on variant pairing of bainitic ferrite in low carbon steel, Acta Mater. 60 (2012) 2387–2396.
[60] G. Miyamoto, N. Iwata, N. Takayama, T. Furuhara, Quantitative analysis of variant selection in ausformed lath martensite, Acta Mater. 60 (2012) 1139–1148.
[61] J. Wang, P.J. van der Wolk, S. van der Zwaag, Determination of martensite start temperature in engineering steels part I. Empirical relations describing the effect of steel chemistry, Mater. Trans. 41 (2000) 761–768.
[62] H.J. Kim, Effects of prior austenite grain size on hydrogen delayed fracture of hot-stamped boron martensitic steel, Metall. Mater. Trans. A 51 (2020) 237–251.
[63] H. Fuchigami, H. Minami, M. Nagumo, Effect of grain size on the susceptibility of martensitic steel to hydrogen-related failure, Philos. Mag. Lett. 86 (2006) 21–29.
[64] H.S. Yang, H.K.D.H. Bhadeshia, Austenite grain size and the martensite-start temperature, Scr. Mater. 60 (2009) 493–495.
[65] S.J. Lee, K.S. Park, Prediction of martensite start temperature in alloy steels with different grain sizes, Metall. Mater. Trans. A 44 (2013) 3423–3427.